Chinese Chemical Letters 34 (2023) 107500

Contents lists available at ScienceDirect

Chinese Chemical Letters

journal homepage: www.elsevier.com/locate/cclet

Surface oxygen-deficient Ti_2SC for enhanced lithium-ion uptake

Jianguang Xu[a,b,*], Hongyan Hang[a], Chen Chen[a], Boman Li[a], Jiale Zhu[a], Wei Yao[a,b,*]

[a] School of Materials Science and Engineering, Yancheng Institute of Technology, Yancheng 224051, China
[b] Key Laboratory for Ecological-Environment Materials of Jiangsu Province, Yancheng Institute of Technology, Yancheng 224051, China

ARTICLE INFO

Article history:
Received 16 March 2022
Revised 27 April 2022
Accepted 7 May 2022
Available online 11 May 2022

Keywords:
MAX phase
Ti_2SC
Oxygen vacancies
Lithium-ion storage
Surface engineering

ABSTRACT

Recently, MAX phases show great potential in lithium-ion uptake due to their excellent electrical conductivity and unique lamellar-structure accommodating lithium ions. However, the reports about MAX electrodes for lithium-ion battery up to now are relatively low. Herein we report the preparation of surface oxygen-deficient Ti_2SC with abundant oxygen vacancies by a facile surface engineering method. When using as a lithium storage anode, this oxygen-deficient Ti_2SC delivers a high capacity of 350 mAh/g at a current density of 400 mA/g as well as excellent rate performance, doubling the capacity compared to that of Ti_2SC without oxygen vacancies. Confirmed by electrochemical impedance spectroscopy (EIS) and kinetic mechanism analyses, after reducing surface oxides and generation of oxygen vacancies, the as-received Ti_2SC exhibits higher electrical conductivity and faster lithium ion diffusion. Thus this work offers a facial and effective strategy of optimizing the surface structure of MAX phases, further to achieve an enhanced lithium-ion uptake for lithium-ion batteries or capacitors.

Due to the quick development of electrical automobile and portable electrical equipment, rechargeable batteries with high energy density and power density received great attention recently [1–4]. Although some novel battery systems have been developed, lithium-ion battery (LIB) is still a reliable and receivable technology for energy storage nowadays [5]. However, the commercial graphic anode for LIB cannot meet the high energy standard due to its low theoretical capacity of 372 mAh/g [5]. Specially, if considering the low tap density of graphite, its ultralow volumetric capacity (330–430 mAh/cm^3) further strongly hinders the development and applications of lithium-ion battery [6]. Thus it is important to find novel anode materials with enhanced lithium-ion storage property.

Recently, layered ternary transition metal carbides or nitrides, also known as MAX phase compounds, showed their promise in lithium-ion storage [7–12]. With the repeating intercalation and de-intercalation of Li^+ ions, the MAX particles have been exfoliated to thin nanosheets due to the structural stress generated by lithiation [7–12], which results in a significant improvement in electrochemical performance of MAX phases. Although their capacities increased with charge/discharge cycling, the close stacked layers and the high electrostatic repulsion between Ti and Li limit the lithiation of MAX phase greatly, rendering the low initial capacity and rate capability [13]. Nano-engineering in their structure is regarded as an effective strategy to increase the utilization of electrodes and achieve better electrochemical performance. For example, we decreased the size of Ti_2SnC, resulting in a high reversible capacity of 430 mAh/g, more than 5 times in comparison with its bulk counterpart [14]. In addition, both partially etched Ti_3AlC_2 [15] and oxidized Ti_3SiC_2 [16] show better specific capacity than their untreated counterparts.

According to the knowledge of fundamentals of material science, introducing defects could increase the conductivity of crystals, and the lithium could be coupled with deficient. It is reported that many metal oxides with oxygen-defects have exhibited obviously improved lithium storage capability [17–19]. MXene, a distinct representative of 2D materials, deriving from their precursor MAX, has lots of surface functional groups such as –O, –F and –OH, which show great efforts on the lithium-ion storage property because the electrical conductivity and surface redox reaction with lithium of MXene are much different with different surface terminations [20–22]. For instance, by regulation of functional groups, high capacity and ultra-long cycle capability of Nb_2CT_x MXene for lithium-ion battery have been achieved [23]. However, there are no reports concerning the surface structure of MAX phase due to the high stability of MAX phase as well as almost no functional groups on its surface. While for most non-oxide ceramics including MAX phase, there are surface oxides covered on their surface in most situations, which would probably influence the electrical conductivity and lithium ions diffusion rate. Therefore, it can be predicted that the electrochemical performance of MAX will be enhanced if the surface structure of MAX has been optimized.

* Corresponding authors.
E-mail addresses: jgxu@163.com (J. Xu), weiyao@ycit.edu.cn (W. Yao).

https://doi.org/10.1016/j.cclet.2022.05.014
1001-8417/

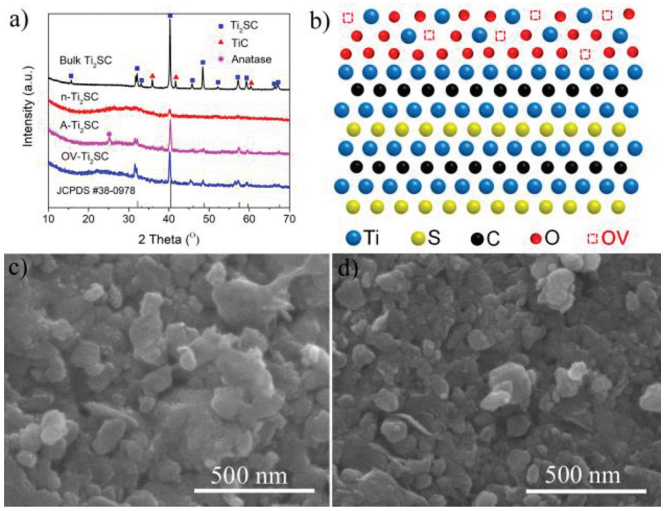

Fig. 1. (a) XRD patterns of Ti_2SC raw materials (bulk Ti_2SC), after ultrasonic exfoliation (n-Ti_2SC), annealing at 400 °C (A-Ti_2SC), annealing with $NaBH_4$ at 400 °C (OV-Ti_2SC). (b) Atomic structure model of Ti_2SC with surface oxide. SEM images of (c) OV-Ti_2SC and (d) A-Ti_2SC.

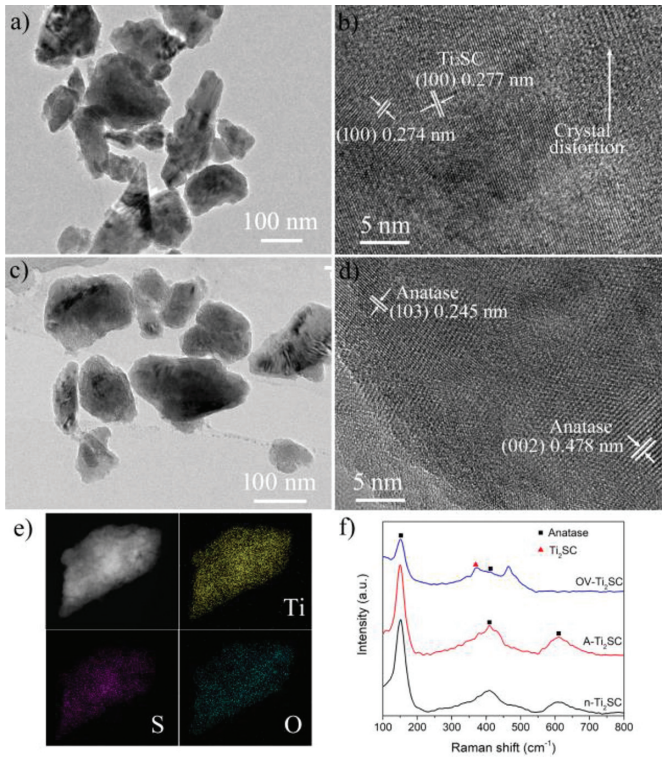

Fig. 2. (a) TEM and (b) HRTEM images of OV-Ti_2SC. (c) TEM and (d) HRTEM images of A-Ti_2SC. (e) Element distribution of OV-Ti_2SC. (f) Raman spectra of different Ti_2SC samples.

Herein we report in a detailed investigation of the lithium-ion storage property of surface oxygen-deficient Ti_2SC nanosheets. By reducing the surface titanium oxide on Ti_2SC particles, oxygen vacancies are generated obviously on their surface. Due to the higher electrical conductivity and Li-ion diffusion rate derived from oxygen vacancies, our surface oxygen-deficient Ti_2SC electrode displays a superior rate performance from 50 mA/g to 2000 mA/g and holds a specific capacity of 350 mAh/g at 400 mA/g after 1000 cycles. These findings further proved the suitability of MAX phase as anode materials for LIB and provided an effective strategy for design surface structure of MAX phase to achieve enhanced electrochemical performance.

Fig. 1 shows XRD patterns and SEM images of different Ti_2SC samples, including Ti_2SC raw materials (bulk Ti_2SC), Ti_2SC collected after ultrasonic exfoliation (n-Ti_2SC), n-Ti_2SC annealed at 400 °C under Ar (A-Ti_2SC), n-Ti_2SC annealed with $NaBH_4$ at 400 °C under Ar (OV-Ti_2SC). According to the XRD pattern in Fig. 1a, it can be concluded that Ti_2SC has been successfully prepared by self-propagating high-temperature synthesis (SHS) method. Besides the main phase Ti_2SC, TiC is also found in this XRD pattern as an impurity phase. After treating by sonication with DMSO, the peaks' intensity became weaker, suggesting Ti_2SC particles are broken or delaminated to small particles or nanosheets. In addition, a broad diffuse hump peak in the region of $2\theta = 20°-35°$ can be also observed, indicating Ti_2SC particles are partially oxidized during sonication. Then after heating at 400 °C for 2 h under Ar, the surface oxides on Ti_2SC particles were crystallized because a new peak at around 26° of anatase TiO_2 appeared. When adding $NaBH_4$ to Ti_2SC during annealing, the hump peak in the region of $2\theta = 20°-35°$ is almost disappeared, showing the oxidized Ti_2SC particles have been partially reduced. Moreover, the peaks of Ti_2SC in XRD patterns of both A-Ti_2SC and OV-Ti_2SC become stronger compared to those of n-Ti_2SC, indicating a crystallization process arisen during annealing.

The atomic model of the lamellar structure of Ti_2SC with surface oxide has been shown in Fig. 1b, which consists of two distinct alternating layers-Ti_2C and S, and surface oxide-titanium oxide with oxygen vacancy. A distinct lamellar structure can be observed in the SEM image (Fig. S1 in Supporting information) of bulk Ti_2SC obtained by SHS, which is consistent with its atomic model. After sonication and annealing, the size of as-synthesized OV-Ti_2SC and A-Ti_2SC powders have been significantly decreased, showing average size of ~100–200 nm (Figs. 1c and d). Moreover, a few ultrathin nanosheets can be also observed in Figs. 1b and c, suggesting successful delamination of bulk Ti_2SC during sonication. In addition, based on EDS results in Table S1 (Supporting information), the atomic O/Ti ratio of OV-Ti_2SC is only 0.116, decreased by 78.4% compared to that of A-Ti_2SC, indicating most surface oxide on Ti_2SC particles has been reduced by adding $NaBH_4$ to Ti_2SC.

Figs. 2a-d show TEM and HRTEM images of OV-Ti_2SC and A-Ti_2SC. Both samples exhibit irregular sheet-like or particle-like morphology with a size range of 100–200 nm, which are consistent with SEM images in Fig. 1. The morphology and size of OV-Ti_2SC and A-Ti_2SC are similar to n-Ti_2SC in Fig. S2 (Supporting information), indicating there are no obvious reactions between particles during annealing. In addition, it can be observed from the edge of both samples that the sheets or particles are composed of a few layers, confirming the lamellar structure of Ti_2SC. According to THE HRTEM images (Figs. 2b and d), the surface of A-Ti_2SC particles are covered by anatase TiO_2, because the spacings of lattice fringes were measured to be 0.245 and 0.478 nm, corresponding to the (103) and (002) crystal plane of anatase TiO_2, respectively [24,25]. However, these lattice fringes of anatase TiO_2 can't be observed on the surface of OV-Ti_2SC particles, while a spacing corresponding to the (100) crystal plane of Ti_2SC was detected in Fig. 2b, suggesting that the surface oxide on OV-Ti_2SC has been partly reduced. In addition, some crystal distortion was found on OV-Ti_2SC particles, which may be ascribed to the residual surface oxide, because the oxygen element is still homogeneously distributed on the surface of OV-Ti_2SC particles according to the element distribution image in Fig. 2e.

The presence of surface oxides on Ti_2SC particles of different Ti_2SC samples is further proved by Raman spectra in Fig. 2f. Three obvious peaks located at 145, 410, 610 cm^{-1} can be observed in the spectra of n-Ti_2SC and A-Ti_2SC, corresponding to the vibration modes of A_{1g}, E_{2g} and E_{2g} of anatase TiO_2, respectively [18,26–28].

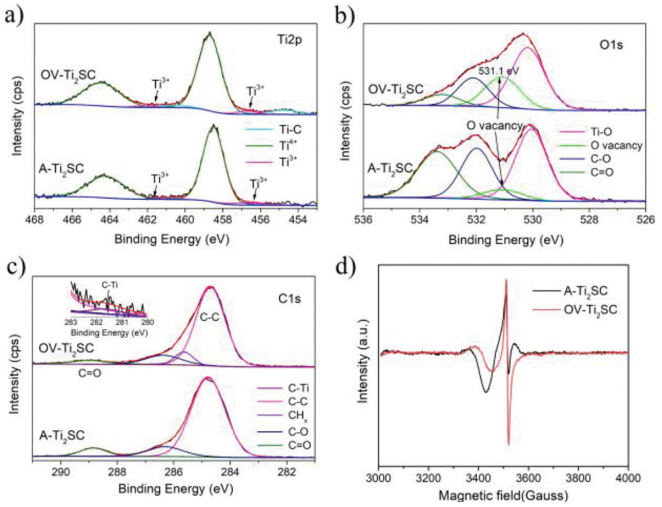

Fig. 3. High resolution (a) Ti 2p, (b) O 1s and (c) C 1s XPS spectra of OV-Ti_2SC and A-Ti_2SC. (d) EPR spectra of OV-Ti_2SC and A-Ti_2SC.

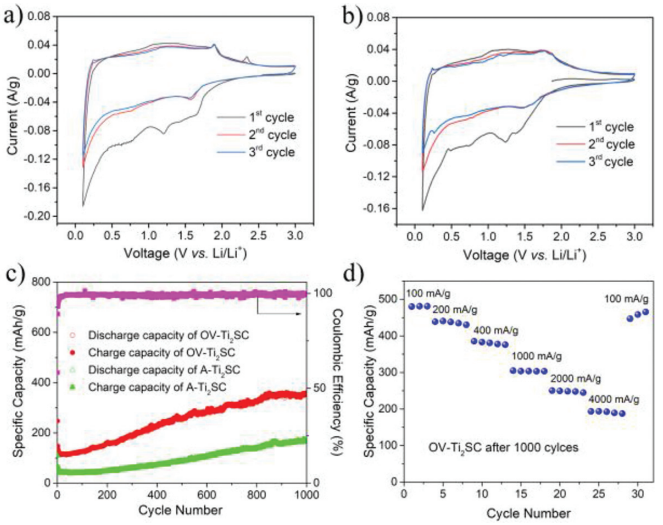

Fig. 4. CV curves of (a) OV-Ti_2SC and (b) A-Ti_2SC nanosheets at a scan rate of 0.1 mV/s. (c) cycle performance and coulombic efficiency of OV-Ti_2SC and A-Ti_2SC at a current density of 400 mA/g. (d) Discharge capacities of OV-Ti_2SC after 1000 charge/discharge cycles under different current densities.

Other two peaks of anatase TiO_2 are not distinct in these spectra, which may be affected by the internal Ti_2SC samples, as the in situ fabricated TiO_2 on Ti_3C_2 MXene [29]. After reducing the surface oxide with $NaBH_4$, the peaks at 410 and 610 cm^{-1} of OV-Ti_2SC were almost disappeared, which can be ascribed to the generation of surface oxygen vacancies [30,31]. At the same time, two peaks at 376 and 460 cm^{-1} became obvious, which are shown as shoulders of the peak at 410 cm^{-1} in the spectra of n-Ti_2SC and A-Ti_2SC. The first one at 376 cm^{-1} is attributed to E_{2g} mode of Ti_2SC, which appeared because part of surface oxide has been reduced [32]. The other one at 460 cm^{-1} are probably from the surface functional -O group on Ti_2SC, because it is located at the region of surface functional groups of Ti_3C_2 MXenes in their Raman spectra, which inherent the metal-carbon bonds of MAX phases [33].

To further study the surface oxidation status of Ti_2SC particles, X-ray photoelectron spectroscopy has been carried and showed in Figs. 3a-c. It can be seen from high resolution XPS patterns of Ti 2p and O 1s of OV-Ti_2SC and A-Ti_2SC (Figs. 3a and b) that there are titanium oxide and carbon oxide covered on the surface of OV-Ti_2SC and A-Ti_2SC particles because the metal-oxygen and carbon-oxygen are the main bonds observed in these spectra. For Ti 2p region of A-Ti_2SC, peaks at 456.5 and 458.3 eV correspond to the different oxidation states of titanium [34–37]. In the Ti 2p region of OV-Ti_2SC, the peak of Ti-C bond (455.6 eV) appeared while the peak of Ti^{3+} (456.3 eV) increased, indicating the decrease of surface oxygen on OV-Ti_2SC flakes. In Fig. 3b, high resolution O 1s spectra of both samples show similar morphology, while the peak of O vacancy (531.0 eV) [38] of OV-Ti_2SC increased a lot compared to that of A-Ti_2SC, indicating the reduction of surface oxides and formation of O vacancy on Ti_2SC particles. The O vacancy is also observed in the EPR spectra of both samples (Fig. 3d), and particularly, the spectrum of OV-Ti_2SC shows a very sharp change at around $g = 2.003$, suggesting there are more O vacancies on the surface of OV-Ti_2SC particles. For comparison, OV-Ti_2SC-300 and OV-Ti_2SC-500 obtained by heating n-Ti_2SC at 300 and 500 °C were also measured by EPR, and the results in Fig. S3 (Supporting information) show that both samples have fewer O vacancies compared to OV-Ti_2SC. High resolution C 1s spectra of OV-Ti_2SC and A-Ti_2SC were fitted to five and three peaks in Fig. 3c, respectively. Three peaks in both samples are assigned to graphitic C-C (284.8 eV), C-O (286.3 eV), and C=O (288.8 eV) bonds [34,35,39]. The other two peaks only in OV-Ti_2SC correspond to internal C—Ti (281.5 eV) and CH_x (285.6 eV) bonds [40], indicating the reduction of surface oxides on Ti_2SC particles. In addition, compared to A-Ti_2SC, the peaks of oxygen-carbon bonds at 286.3 eV and 288.8 eV for OV-Ti_2SC decreased a lot, consistent with the results of O 1s spectra, further proving the reduction effect during heating with $NaBH_4$. Thus combining the results of XRD, EDS, TEM, Raman, XPS and EPR, the surface oxides on Ti_2SC particles are mainly composed of anatase TiO_2, and which are partly reduced after annealing n-Ti_2SC with $NaBH_4$ under Ar as well as generation of oxygen vacancies. Here $NaBH_4$ is applied as a reduction agent, which can be decomposed at high temperature and provides active hydrogen that will create oxygen vacancies on the surface of Ti_2SC. [41] In addition, as well known, XPS analysis is sensitive to surface structure while EPR displays the bulk oxygen vacancy [18,42], thus oxygen vacancies should be located both on the surface and in the bulk of the anatase layer.

Figs. 4a and b show the initial three CV curves of OV-Ti_2SC and A-Ti_2SC anodes, which have similar morphology. In the course of the 1st cathodic scan, the small reduction peak at around 1.65 V (*vs.* Li/Li^+) associates with the establishment of Li_xTiO_2 [18,31], while two wide reduction peaks, positioned at 1.21 and 0.72 V (*vs.* Li/Li^+), suggest the setting up of a solid electrolyte interface (SEI) layer. Moreover, the oxidation peak, located at 1.90 V (*vs.* Li/Li^+), conforms with the reversible processes of Li_xTiO_2 to TiO_2 with the Li-ions deintercalation from Ti_2SC [18,31]. Compared to A-Ti_2SC, the pair of redox peaks at 1.65 and 1.90 V (*vs.* Li/Li^+) of OV-Ti_2SC are sharper during all the initial three cycles, suggesting the redox reaction between Li_xTiO_2 and TiO_2 is easier on the surface of OV-Ti_2SC particles, which may be attributed to faster Li ions diffusion in the structure with abundant oxygen vacancy. In addition, an oxidation peak close to 2.34 V (*vs.* Li/Li^+) can be observed in the first CV curve of OV-Ti_2SC, which may be induced by the sulfur residue arisen from the delamination solvent DMSO and exposed after reduction of surface oxides [14]. The existence of sulfur residue is also proved by high resolution S 2p XPS spectrum of OV-Ti_2SC in Fig. S4 (Supporting information) because S-S bonds at 164.4 and 165.7 eV can be observed in this spectrum [43,44].

Fig. 4c shows the cyclic profiles of OV-Ti_2SC and A-Ti_2SC electrodes at 400 mA/g. The 1st lithiation capacity of OV-Ti_2SC is 247 mAh/g, while the 2nd lithiation capacity is decreased to 148 mAh/g. This capacity loss can be ascribed to the irreversible setting up of a SEI layer. After the initial a few charge/discharge cycles, the

specific capacity begins to gradually grow with cycling and then a stable reversible capacity of 350 mAh/g has been reached after ~820 cycles. The coulombic efficiency of the first cycle is 58%, then achieved to close 100% after a few cycles and persisted unchangeable in the following cycles. This increase in lithium ions storage with cycling can be assigned to the thinner nanosheets exfoliated by constant insertion of Li^+, bringing about much more electrochemical active sites on the surface for Li^+ insertion and alloying [7,8,14]. On the other hand, the A-Ti_2SC anode with less oxygen vacancy displays a capacity of 170 mAh/g after 1000 charge/discharge cycles, which is far smaller than that of the OV-Ti_2SC anode. The higher capacity of OV-Ti_2SC anode could be attributed to its specific surface structure with abundant oxygen vacancies, facilitating the diffusion and intercalation of lithium ions into OV-Ti_2SC particles. Moreover, OV-Ti_2SC electrode also displays excellent long-term cyclic performance at a high current density of 4 A/g, and a stable reversible capacity of 130 mAh/g is still preserved even after 3000 charge/discharge cycles (Fig. S5 in Supporting information). The stability of OV-Ti_2SC electrode in the process of cycle performance is further proved by the EPR results of different charge/discharge cycles, showing in Fig. S6 (Supporting information). The intensity of EPR peaks is increased after 100 charge/discharge cycles, and then kept stable even after 1000 charge/discharge cycles, indicating bulk O vacancies are increased with initial a few cycles and then remained almost no change during following cycles.

Fig. 4d shows the rate performance of OV-Ti_2SC after 1000 charge/discharge cycles at different current densities. At the current density of 100 mA/g, the OV-Ti_2SC electrode delivers a reversible specific capacity of 480 mAh/g. When the current densities were increased to 200, 400, 1000, 2000 and 4000 mA/g, the OV-Ti_2SC electrode exhibits reversible capacities of 432, 377, 303, 245 and 190 mAh/g, respectively. In addition, the OV-Ti_2SC electrode recovers a specific capacity of ~466 mAh/g once the current density was restored to 100 mA/g, exhibiting a splendid rate performance. Comparison of the rate performance between fresh OV-Ti_2SC and A-Ti_2SC without any previous charge/discharge cycles is shown in Fig. S7 (Supporting information). The capacities of fresh OV-Ti_2SC are much higher than those of A-Ti_2SC, particularly in high current density, indicating the higher electrical conductivity and the faster lithium ion diffusion in the OV-Ti_2SC electrode. In addition, the rate and cyclic performance of OV-Ti_2SC-300 and OV-Ti_2SC-500 are also presented in Figs. S7 and S8 (Supporting information), respectively. Due to their fewer O vacancies, both samples show poorer electrochemical performance compared to OV-Ti_2SC. Thus it can be concluded that the number of oxygen vacancies has great impact on the electrochemical performance of Ti_2SC.

Moreover, electrochemical impedance spectroscopy (EIS) was performed to analyze the electrochemical behavior of both Ti_2SC anodes. It can be seen from Fig. S9 (Supporting information), both Nyquist plots are mainly composed of two parts: a semicircle in the high frequency region is considered as the resistance at the Ohmic surface layer, and an oblique line in the low frequency region represents an ion diffusion process. To quantitatively asses the two processes, the Nyquist plots were fitted using the modified Randles equivalent circuit (the inset in Fig. S9). On the basis of the fitting results, the OV-Ti_2SC anode exhibits a lower charge-transfer resistance of 291.7 Ω, while A-Ti_2SC shows a higher transfer resistance of 410.3 Ω, indicating the oxygen vacancy enhances the electrical conductivity significantly and as a result, OV-Ti_2SC anode reaches a faster charge-transfer procedure. This finding is in a good agreement with the improvement of electrochemical performance of OV-Ti_2SC anode.

To further explain the reasons in detail for the splendid electrochemical behavior, particularly the rate behavior of the OV-Ti_2SC electrode, the kinetic mechanism analyses were performed according to its CV measurement. Figs. S10a and b (Supporting information) exhibit the CV profiles of OV-Ti_2SC and A-Ti_2SC at the scan rates from 0.1 mV/s to 2 mV/s, respectively. On the basis of the model of Dunn [45], the current in CV curve is divided into two fractions, associating with two different mechanisms, the surface-induced capacitive process and the diffusion-controlled insertion/extraction process. The formula: $i = a\nu^b$, in which both a and b are constants, representing the power law relationship between current (i) and the scan rate (ν), is applied to qualitatively examine the contribution of the two processes. The b value can be calculated by the slope of the fitted line $\log(\nu)$-$\log(i)$ (i = peak current). A b value of 0.5 means a typical diffusion-controlled mechanism, while b value of 1.0 is considered as surface-controlled capacitance behavior [46]. The b values of cathodic/anodic process are calculated to be 0.829/0.842 and 0.822/0.824 for OV-T_2SC and A-Ti_2SC, respectively (Figs. S10c and d in Supporting information). Compared with A-Ti_2SC electrode, the larger b values obtained in OV-T_2SC electrode are associated with more capacitive-like behaviors, befitting to faster reaction kinetics, which is useful for achieving superior rate performance. The quantitative capacitive contribution can be further analyzed according to the equation $i(V) = k_1\nu + k_2\nu^{0.5}$, where $k_1\nu$ is ascribed to surface-controlled capacitive contribution, $k_2\nu^{0.5}$ is associated with diffusion-controlled insertion process, both k_1 and k_2 are constants, ν is the scan rate, and i is the current at a fixed potential (V) [45]. Thus the contribution of capacitive-like behavior for the OV-T_2SC electrode is as high as 78.2% at 0.5 mV/s (Fig. S10e in Supporting information), which is bigger than that for the A-T_2SC electrode (Fig. S10f in Supporting information), showing a better rate performance as a result. In addition, the capacitive contribution of A-T_2SC and OV-Ti_2SC at other scan rates was also calculated and shown in Fig. S11 (Supporting information). The fraction of capacitive contribution increases with the scan rate, and the overall contribution of OV-Ti_2SC at all scan rates is higher than A-T_2SC, further indicating the fast redox reaction behavior of OV-Ti_2SC.

Interestingly, OV-Ti_2SC electrode renders a high capacity of ~350 mAh/g after 1000 charge/discharge cycles at a current density of 400 mA/g, which doubles the values of A-Ti_2SC and our previous result of submicron Ti_2SC [7], further confirming the lithium-ion storage potential of MAX phase compounds. The Li-ion uptake in MAX phase compounds was proved to be originated from the intercalation of Li-ion into the layer structure of MAX phase because there are strong interactions of MX-Li and A-Li, specially for A elements (Si, Sn, S and so on) having alloying effects with lithium [9]. Assuming two Li ions can intercalate next to S atom in MAX phase, theoretical capacity value of 383 mAh/g can be expected for Ti_2SC, which is in good agreement with the OV-Ti_2SC electrode. The increased specific capacity and better rate performance of OV-Ti_2SC may attributed to the partly reduced surface oxides and generation of O vacancies on Ti_2SC particles, which provide better electrical conductivity and surface-induced capacitive contribution. In addition, it's worth mentioning that the high specific capacity of 480 mAh/g at 100 mA/g is highly comparable with those of previously reported MAX materials, showing in Fig. S12 (Supporting information). Especially at a high current density of 2000 mA/g, OV-Ti_2SC electrode has the highest specific capacity of 245 mAh/g among all reported MAX materials.

In summary, we prepared surface oxygen-deficient Ti_2SC by annealing the sonication delaminated Ti_2SC with $NaBH_4$. Benefiting from reduction of surface oxides and generation of oxygen vacancies, the as-prepared oxygen-deficient Ti_2SC (OV-Ti_2SC) shows a higher lithium-ion storage capacity and a better rate capability compared to Ti_2SC with more surface oxides. A specific capacity of 350 mAh/g for OV-Ti_2SC, along with impressive cycling performance and excellent rate capability were achieved, showing the promise of MAX phase for Li uptake. Considering there

is a large amount of MAX phase compounds, this research provides a promising, facile surface engineering strategy for exploring the lithium-ion storage property of 2D materials from this large family.

Declaration of competing interest

The authors declare that they have no known competing financial interests or personal relationships that could have appeared to influence the work reported in this paper.

Acknowledgments

This work was supported by the National Natural Science Foundation of China (Nos. 21671167 and 51602277), Qinglan Project of Jiangsu Province. In addition, the authors would like to thank Shiyanjia Lab (www.shiyanjia.com) for the support of Raman and EPR analysis.

Supplementary materials

Supplementary material associated with this article can be found, in the online version, at doi:10.1016/j.cclet.2022.05.014.

References

[1] Y. Zhang, L. Tao, C. Xie, et al., Adv. Mater. (2020) 1905923.
[2] A. Bhargav, J. He, A. Gupta, et al., Joule 4 (2020) 285–291.
[3] T. Kwon, J.W. Choi, A. Coskun, Joule 3 (2019) 662–682.
[4] J. Xu, M. Jin, X. Shi, et al., Nanomaterials 11 (2021) 2279.
[5] T. Kim, W. Song, D. Son, et al., J. Mater. Chem. A 7 (2019) 2942–2964.
[6] N. Nitta, F. Wu, J.T. Lee, et al., Mater. Today 18 (2015) 252–264.
[7] J. Xu, M. Zhao, Y. Wang, et al., ACS Energy Lett. 1 (2016) 1094–1099.
[8] S. Zhao, Y. Dall Agnese, X. Chu, et al., ACS Energy Lett. 4 (2019) 2452–2457.
[9] Y. Li, G. Ma, H. Shao, et al., Nano-Micro Lett. 13 (2021) 158.
[10] X. Xie, S. Wang, K. Kretschmer, et al., J. Colloid Interface Sci. 499 (2017) 17–32.
[11] A.T. Tesfaye, Y. Gogotsi, T. Djenizian, Electrochem. Commun. 81 (2017) 29–33.
[12] A. Sengupta, B.V.B. Rao, N. Sharma, et al., Nanoscale 12 (2020) 8466–8476.
[13] J. Zhu, A. Chroneos, L. Wang, et al., Appl. Mater. Today 9 (2017) 192–195.
[14] H. Wu, J. Zhu, L. Liu, et al., Nanoscale 13 (2021) 7355–7361.
[15] X. Chen, Y. Zhu, X. Zhu, et al., ChemSusChem 11 (2018) 2677–2680.
[16] S. Luan, J. Zhou, Y. Xi, et al., ChemistrySelect 4 (2019) 5319–5321.
[17] Z. Hao, Q. Chen, W. Dai, et al., Adv. Energy Mater. 10 (2020) 1903107.
[18] Y. Xie, D. Hu, L. Liu, et al., J. Hazard. Mater. 318 (2016) 551–560.
[19] J. Mei, Y. Zhang, T. Liao, et al., National Sci. Rev. 5 (2018) 389–416.
[20] C. Wang, S. Chen, L. Song, Adv. Func. Mater. 30 (2020) 2000869.
[21] X. Zha, K. Luo, Q. Li, et al., EPL 111 (2015) 26007.
[22] R. Ibragimova, P. Erhart, P. Rinke, et al., J. Phys. Chem. Lett. 12 (2021) 2377–2384.
[23] J. Zhao, J. Wen, J. Xiao, et al., J. Energy Chem. 53 (2021) 387–395.
[24] L. Wang, G. Yang, J. Wang, et al., Small 15 (2019) 1901584.
[25] H. Yuan, R. Besselink, Z. Liao, et al., Sci. Rep. 4 (2015) 4584.
[26] R. Zheng, C. Shu, Z. Hou, et al., ACS Appl. Mater. Interfaces 11 (2019) 46696–46704.
[27] M. Cao, F. Wang, L. Wang, et al., J. Electrochem. Soc. 164 (2017) A3933–A3942.
[28] X. Li, X. Yin, M. Han, et al., J. Mater. Chem. C 5 (2017) 4068–4074.
[29] X. Zhang, Y. Liu, S. Dong, et al., Ceram. Int. 43 (2017) 11065–11070.
[30] J. Qiu, S. Li, E. Gray, et al., J. Phys. Chem. C 118 (2014) 8824–8830.
[31] J. Zheng, L. Liu, G. Ji, et al., ACS Appl. Mater. Interfaces 8 (2016) 20074–20081.
[32] T.H. Scabarozi, S. Amini, P. Finkel, et al., J. Appl. Phys. 104 (2008).
[33] A. Sarycheva, Y. Gogotsi, Chem. Mater. 32 (2020) 3480–3488.
[34] J. Xu, J. Zhu, C. Gong, et al., Chin. Chem. Lett. 31 (2020) 1039–1043.
[35] Z. Wang, Z. Xu, H. Huang, et al., ACS Nano 14 (2020) 4916–4924.
[36] Z. Zhang, Z. Yao, X. Zhang, et al., Electrochim. Acta 359 (2020) 136960.
[37] S. Wang, M. Xu, T. Peng, et al., Nat. Commun. 10 (2019) 676.
[38] Z. Chen, L. Xu, Q. Chen, et al., J. Mater. Chem. A 7 (2019) 6740–6746.
[39] S. Yazdanparast, S. Soltanmohammad, A. Fash-White, et al., ACS Appl. Mater. Interfaces 12 (2020) 20129–20137.
[40] M. Han, K. Maleski, C.E. Shuck, et al., J. Am. Chem. Soc. 142 (2020) 19110–19118.
[41] D. Ariyanti, L. Mills, J. Dong, et al., Mater. Chem. Phys. 199 (2017) 571–576.
[42] J. Li, M. Zhang, Z. Guan, et al., Appl. Catal. B: Environ. 206 (2017) 300–307.
[43] W. Bao, C.E. Shuck, W. Zhang, et al., ACS Nano 13 (2019) 11500–11509.
[44] D.K. Lee, Y. Chae, H. Yun, et al., ACS Nano 14 (2020) 9744–9754.
[45] V. Augustyn, J. Come, M.A. Lowe, et al., Nat. Mater. 12 (2013) 518–522.
[46] F. Wu, S. Zhang, B. Xi, et al., Adv. Energy Mater. 8 (2018) 1703242.